

# Strong-field ionization of H<sub>2</sub> from ultraviolet to near-infrared wavelengths: Photoelectron energy and angular identifications

Timo Wilbois\* and Hanspeter Helm†

*Department of Molecular and Optical Physics, University of Freiburg, Stefan-Meier-Strasse 19, D-79104 Freiburg, Germany*

(Received 18 July 2011; published 11 November 2011)

Strong-field ionization of molecular hydrogen is studied at wavelengths ranging from 300 to 800 nm using pulses of 100-fs duration. We find that over this wide wavelength range, from nominally 4-photon to 11-photon ionization, resonance features dominate the ionization probability at intensities below  $10^{14}$  W/cm<sup>2</sup>. Photoelectron momentum maps recorded by an imaging spectrometer are analyzed to identify the wavelength-dependent ionization pathways in single ionization of molecular hydrogen. A number of models, some empirical, which are appropriate for a quantitative interpretation of the spectra and the ionization yield are introduced. A near-absolute comparison of measured ionization yields at 398 nm is made with the predictions based on a numerical solution [Y. V. Vanne and A. Saenz, *Phys. Rev. A* **79**, 023421 (2009)] of the time-dependent Schrödinger equation for two correlated electrons.

DOI: 10.1103/PhysRevA.84.053407

PACS number(s): 33.80.Rv

## I. INTRODUCTION

The topic of molecular hydrogen in strong laser fields has received continued attention in theory [1–8] and experiment [9–17]. A preponderance of short-pulse experiments on H<sub>2</sub> has been conducted at wavelengths near 800 nm, many concentrating on the question of double ionization of the neutral molecule or ionization and dissociation of the molecular ion [17–24]. A few dealt explicitly with ac Stark shifting of intermediate resonance states and their identification [25–30]. The latter has been a broad topic in nanosecond and picosecond multiphoton experiments [31–38].

In long-pulse ionization at moderate intensities resonances, isolated in frequency space, dominate the ionization rate and the photoelectron momentum spectra. In short-pulse strong-field ionization, on the other hand, the ground-state electron wave function is projected into an excited-state manifold that is continuously modified during the laser pulse. This dynamic response is mirrored in the photoelectron momentum spectra in islands of resonant ionization in specific intensity ranges and less structured nonresonant ionization patterns. This distinction is possible because the electron energy *at birth* can be recorded at pulse durations that inhibit the recovery of ac Stark energies [39–42]. Insignificant recovery occurs when the electron cannot experience the full spatial profile of the laser beam during its drift toward the detector [40]. While it may not be surprising that the very same resonance states that appear in long-pulse ionization at moderate intensities will also contribute to strong-field ionization, modifications due to ac Stark shifting, above-threshold ionization, and the gradual transition to tunnel ionization affect events, and the strongest channels will dominate individual spectra as the typical experiment integrates [43] over the ionization volume and pulse envelope.

The work here aims at illuminating the ac Stark modified excited state and continuum manifold in molecular hydrogen over a wide wavelength range, from nominally 4-photon to

11-photon ionization. We deduce common traits and rules from these spectra and their identification. These data help in clarifying the molecular ion states that are prepared at the various wavelengths in typical strong-field experiments. They also represent a database against which advanced theoretical models of short-pulse ionization can be tested.

## II. BACKGROUND

Singlet states emerging from the H(1s) + H ( $n = 3, \ell$ ) and H(1s) + H ( $n = 4, \ell$ ) dissociation limits give rise to the strongest visible and near-UV emission bands in molecular hydrogen, the  $3d \leftrightarrow 2p$  and  $4d \leftrightarrow 2p$  Rydberg-Rydberg transitions. Their potential energy curves are shown in detail in Fig. 1.

They reveal the well-studied modification by long-range ion-pair and doubly-excited character, leading in some cases to double minima potentials. The lowest 11 Rydberg states of singlet H<sub>2</sub> are the  $^1\Sigma_g^+$  states, *EF*, *GK*, *H $\bar{H}$* , *P*, and *O*, the long-range ion-pair state,  $B^1\Sigma_u^+$  and its higher analogs, *B'*, *B''*, and *B4*, and the  $^1\Pi_u$  states, *C* and *D*. Their potential energy curves have been calculated to very high precision by Dressler, Wolniewicz, and coworkers [44,45], whose state notation we use here. These states also play a decisive role as intermediate states in multiphoton ionization of H<sub>2</sub>. For this reason we also show in Fig. 1 the vibrational wave function of ground-state H<sub>2</sub> and its associated potential energy curve, both shifted up in energy by six photons at the example of  $\lambda = 470$  nm. The role of these lowest singlet states is particularly pronounced at shorter wavelengths, when a single photon suffices to ionize the resonant intermediate.

At longer wavelengths higher Rydberg states are dominant intermediaries. The reason is that, in atomic hydrogen, the transition dipole moments  $\langle n, \ell | \mathbf{r} | n', \ell + 1 \rangle$  exceed by typically an order of magnitude those of  $\langle n, \ell | \mathbf{r} | n', \ell - 1 \rangle$ , thus favoring higher  $\ell$  and, consequently, higher  $n$  states as intermediaries. This fact is well documented in short-pulse, strong-field resonance switching, which revealed the importance of *4f*, *5f*, and *5g* states in rare-gas and atomic hydrogen ionization [40,46,47].

\*wilbois@cip.physik.uni-freiburg.de

†helm@uni-freiburg.de



electrons around the laser polarization axis this geometry enables the deconvolution of the measured two-dimensional (2D) image to infer the three-dimensional (3D) distribution of photoelectron momenta. If not otherwise noted, we use the algorithm introduced by Bordas *et al.* [51], frequently referred to as onion peeling.

Ionic fragments are detected by a channeltron for time-of-flight measurement. Electrostatic lenses are used to focus ions toward the channeltron in order to enable detection of energetic ions from dissociation. The geometry permits  $4\pi$  detection of ion kinetic energies of up to 13 eV.

#### IV. EXPERIMENTAL RESULTS AND DISCUSSION

##### A. Wavelengths between 300 and 332 nm

Figures 4–7 show experimental results obtained in this wavelength range. We begin with a discussion of marked photoelectron features and their relation to the energy diagram in Fig. 2. A very prominent peak appears at the shortest wavelength, at 300 nm, near 1-eV electron energy; see the solitary ring in Fig. 4(a).

It arises from resonant  $(3 + 1)$ -photon ionization via the  $C^1\Pi_u$  ( $v = 0$ ) state. Owing to the similarity of the equilibrium separations of  $C$  state and the ground state of  $H_2^+$  the dominant final level in this channel is  $H_2^+$  ( $v^+ = 0$ ).

All peaks at energies  $< 1$  eV that appear at the wavelengths shown in Fig. 4 are also due to  $(3 + 1)$ -photon ionization. These peaks arise from ionization via intermediate vibrational levels of the  $B^1\Sigma_u^+$  state and involve changes of vibrational level in the ionization step. Proof for the involvement of the  $B$  state is that these lower-energy peaks remain in the spectra at wavelengths longer than 300 nm, even as the signature of  $C^1\Pi_u$  ( $v = 0$ ) fades; see the angle-integrated spectra in Fig. 5.

Modeling the location of the lower-energy photoelectron peaks in Fig. 5 on the basis of this assignment requires a judgment of the relative importance of nonresonant ionization (NRI) and  $(3 + 1)$ -photon resonant ionization (RI) via a  $B$ -state level. Signatures expected from nonresonant ionization are shown by the red bars in Fig. 5 and by the red line in Fig. 6. The resonant contribution of the  $B$  state ( $v_B = 8$ ) is shown in black, and the summed signal is shown in blue. This simulation

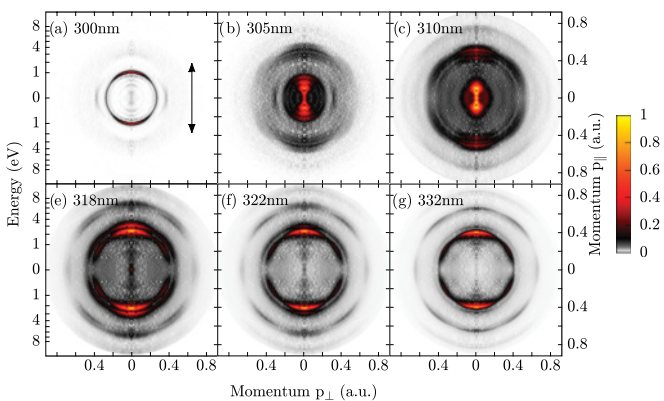


FIG. 4. (Color online) Photoelectron momentum maps recorded at a peak intensity of  $\mathcal{I} \approx 1.5 \times 10^{13}$  W/cm<sup>2</sup>. The orientation of the linear laser polarization is marked in the first plot by the arrows.

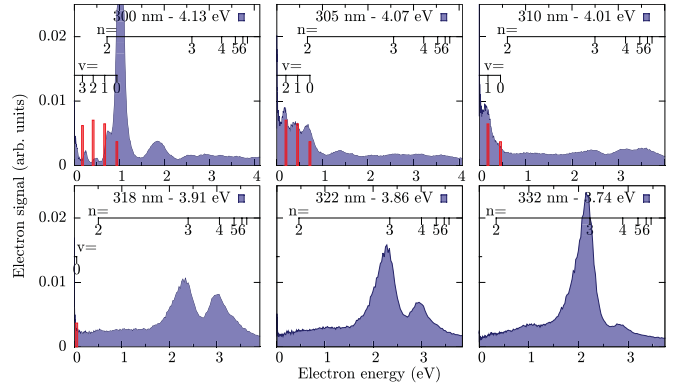


FIG. 5. (Color online) Angle-integrated photoelectron energies recorded at a peak intensity of  $\mathcal{I} \approx 1.5 \times 10^{13}$  W/cm<sup>2</sup> and wavelengths between 300 and 332 nm. Red bars indicate energies and Frank-Condon factors for nonresonant ionization at this intensity. Black bars mark energies expected for ionization via Rydberg states of principal quantum number  $n$  according to Eq. (3).

requires relative electronic  $n$ -photon transition rates,  $R^{(n)}$ . The  $(3 + 1)$ -photon resonant rate (with  $v_B = 8$ ) is taken as

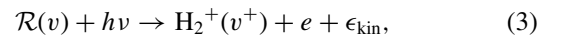
$$\Gamma_{\text{RI}} = R^{(3)} \sum_{v_+} F_{v=0, v_B} F_{v_B, v^+}, \quad (1)$$

the nonresonant four-photon ionization rate is taken as

$$\Gamma_{\text{NR}} = R^{(4)} \sum_{v_+} F_{v=0, v^+}, \quad (2)$$

each weighted by the respective squared Frank-Condon factors  $F_{v, v'}$ . For the model simulation in Fig. 6 we used the empirical ratio  $R^{(3)}/R^{(4)} = 15$  to match the experimental data. The width of the resonant peaks was taken as equal to the laser bandwidth,  $\sigma = 3$  nm, and the width of the nonresonant contributions was taken as  $\sqrt{4}\sigma$ . The model predictions are slightly high in energy by about 50 mV.<sup>1</sup>

A localization of photoelectrons at practically one distinct kinetic energy, as for ionization via the  $C$  state at 300 nm, also appears at 332 nm. Here the peak is localized near 2 eV; see Fig. 4(g). In the range between 332 and 318 nm,  $(4 + 1)$ -photon ionization channels via intermediate Rydberg states  $n = 3, 4$ , and 5 over a range of vibrational levels are active. The vibrational structure is, however, not apparent. This is due to the fact that spectral simplification occurs when the Rydberg potential is close to that of the molecular ion. In this case the vibrational quantum number is preserved, and the electron energy remains close to that of the respective atomic hydrogen excited state when molecular states with small quantum defect  $\delta$  are ionized. Electrons formed in one-photon ionization of a vibronic state  $\mathcal{R}(v)$ ,



<sup>1</sup>A likely reason for this shift in energy is bound-bound transitions between the  $C$  and  $B$  states and the respective  $n = 5, 6$  Rydberg states as these are near resonant at 300 nm. Our 11-state model [48] could readily be extended to include these higher Rydberg states for an explicit prediction; however, the lack of precise transition moments does not warrant such an extension at this point.

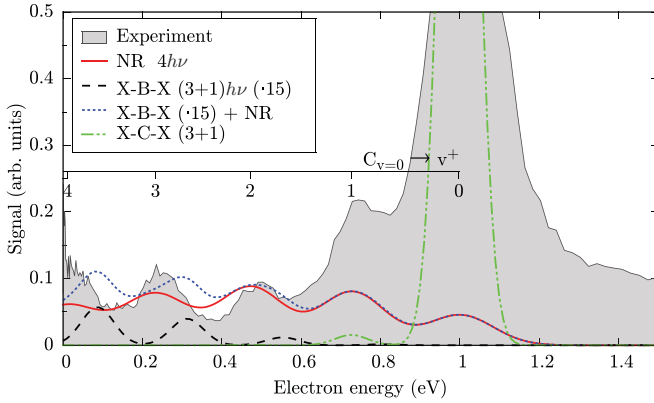


FIG. 6. (Color online) Electron energy distribution at 300 nm, at a peak intensity of  $\approx 1.5 \times 10^{13}$  W/cm<sup>2</sup>. The predicted peak locations from nonresonant ionization are shown in red (solid), and those from the *B* state intermediate level,  $v_B = 8$ , are in black (dashed). The sum of both is given in blue (dotted). Positions for  $C^1\Pi_u(v=0) \rightarrow v^+$  are given also, with the contribution predicted for the *C* state being given by the green (dash-dotted) trace.

where  $v = v^+$ , produce photoelectrons at the kinetic energy  $\epsilon_{\text{kin}} = 0.5(n + \delta)^{-2} + h\nu$ , where  $n$  is the principal quantum number of the Rydberg state. This simplification had previously been reported in picosecond ionization [31] and may be seen as a consequence of the weak dependence of quantum defects on the internuclear distance for the molecular Rydberg states with a higher angular momentum quantum number. The broadening of peaks in Fig. 5 may be attributed to the spread of quantum defects of the involved states [52].

We note that in excitation channels with an *even* number of photons (four photons in Fig. 5) a dominance of *odd* principal quantum numbers (here  $n = 3$ ) is observed. The reason is the preferred access to the the highest angular momentum state, a

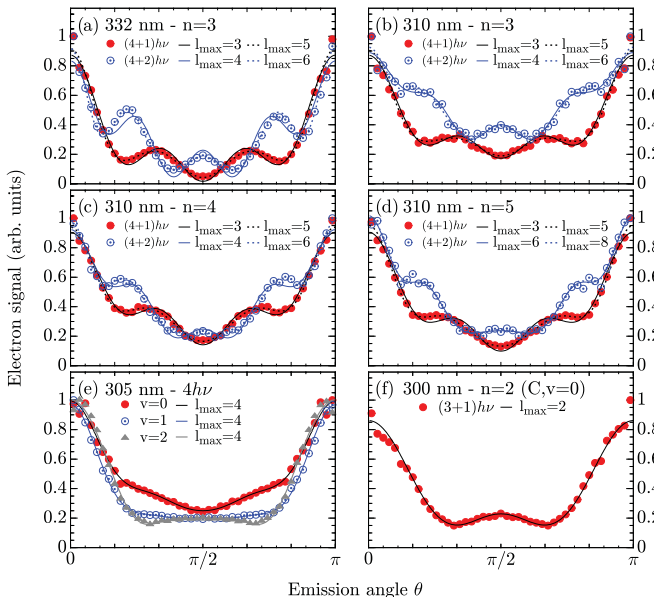


FIG. 7. (Color online) Angular distributions for selected energies in spectra from 332 to 300 nm. Dots represent experimental data, and solid lines are from fits with Legendre polynomials according to Eq. (4) with  $l_{\text{max}}$ , as indicated in the graphs.

point to which we return later. It may also be worth mentioning that at wavelengths below 322 nm the resonant intermediates already lie above the ionization threshold, but one-photon ionization dominates over vibrational autoionization of these four-photon excited levels.

A second piece of information to consider is contained in the angular distribution of the photoelectrons. The distribution associated with the 1-eV peak at 300 nm is readily explained. Three-photon excitation of the  $C^1\Pi_u$  state prepares a  $p_z$  orbital oriented along the polarization axis.

Ionization by the fourth photon accesses *s* and *d* channels of the outgoing electron. This is precisely what is being observed in Fig. 7(f). The experimental distribution for a specific energy channel  $d\epsilon$  can be well reproduced by the formula [53]

$$\frac{df}{d\epsilon d\theta} = \sum_{l=0}^{l_{\text{max}}} \beta_{2l} P_{2l}^0(\theta), \quad (4)$$

with  $P_\ell^m(\theta)$  being the associated Legendre polynomials and  $\theta$  being the angle of the outgoing electron measured relative to the laser polarization axis.

Similar qualitative arguments can be made at the longer wavelengths for the peaks that appear at the positions  $n = 3, 4, 5$ . In this case four-photon excitation prepares intermediate states with *even* angular momentum. Adding one additional photon releases a continuum electron of *odd* angular momentum. This is apparent from the red dots in Figures 7(a)–7(d), which all show a pronounced minimum at  $\theta = \pi/2$  and a shape dominated by *f* character,  $\ell = 3$ . By the same token the respective first above-threshold ionization (ATI) peaks all show a maximum at  $\theta = \pi/2$  and a shape dominated by *g* character,  $\ell = 4$ , as expected.

No simple explanation is at hand for the angular distributions of the low-energy peaks ( $< 1$  eV) at 305 nm, which are shown in Fig. 7(e). These peaks arise from NRI and RI via the *B* state.

## B. Wavelengths near 400 nm

The energy of  $C^1\Pi_u(v=0)$  is nearly degenerate with the opposite parity state,  $E, F^1\Sigma_g^+(v=0)$ , with the *E, F* state level lying higher by 9.1 meV [54]. The one-photon ionization threshold for *E, F* ( $v=0$ ) is at  $\lambda = 396$  nm. With ponderomotive shifting the *E, F* ( $v=0$ ) state becomes resonant with four photons at  $\sim 1.7 \times 10^{13}$  W/cm<sup>2</sup> at  $\lambda = 396$  nm. This resonant (4 + 1)-photon ionization path appears only at the lowest intensities and only at wavelengths  $\leq 396$  nm, barely visible as the central spot at near-zero electron energy in Figs. 8(a) and 8(b).

Stronger contributions appear at energies  $< 200$  meV at low intensities. They are due to nonresonant five-photon ionization, the region marked by blue squares. These contributions mark the intensity-dependent channel closing for the nonresonant process, which is indicated by the red line labeled  $v^+ = 0$  in Fig. 9. The ionization potential of  $\text{H}_2$ , 15.43 eV [55], corresponds to five photons of 401.8 nm. For a wavelength of 396 nm, five photons are sufficient to populate the vibrational ground state of  $\text{H}_2^+$ , at intensities up to  $10^{13}$  W/cm<sup>2</sup>, when the ponderomotive shift amounts to  $\sim 150$  meV. In this way,  $\text{H}_2^+$  can be produced selectively in the vibrational ground state.

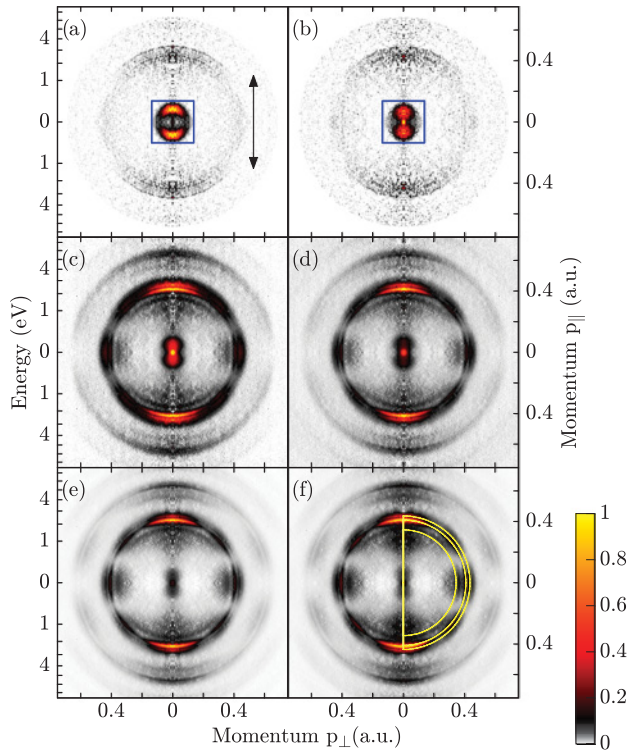


FIG. 8. (Color online) Photoelectron momentum maps recorded at 396 nm at (a) 0.7, (b) 1.1, (c) 2.1, (d) 2.8, (e) 3.9, and (f)  $5.9 \times 10^{13}$  W/cm<sup>2</sup>.

From the data marked by the blue rectangles in Figs. 8(a) and 8(b) we measured the contribution of ions in the vibrational ground state by detecting single electron hits. At 396 nm the five-photon channel to H<sub>2</sub><sup>+</sup>( $v^+ = 0$ ) amounts to >61% at 7 TW/cm<sup>2</sup> and to >47% at 11 TW/cm<sup>2</sup>, with the greater sign indicating that the ATI contributions will most likely also favor the  $v = 0$  channel.

The data in Fig. 9 were recorded at  $\lambda = 398$  nm, where no contribution from  $E,F$  ( $v = 0$ ) appears. At higher intensities the 5-photon channel is superseded by strong  $(5 + 1)$ -photon channels with discrete energy release, corresponding to ionization of molecular Rydberg states with  $n = 3, 4, 5$ . They ionize preferentially in vibrationally diagonal transitions, close to the ionization potential of the respective atomic states, thus giving rise to photoelectron energies according to Eq. (3).

The map of electron energy versus intensity at 398 nm in Fig. 9 shows that now the  $n = 4$  channel dominates. This is opposite to the finding at shorter wavelengths [see Figs. 5(e), 5(f), and 5(g)] when  $n = 3$  states dominate. We recognize from the energy diagram in Fig. 2 that near 400 nm, the higher vibrational levels of  $n = 3, v = 2, 3$ , could act as intermediates, yet  $n = 4$  dominates at this wavelength. This dominance is attributed to the ease at which the highest angular momentum state,  $\ell = 3$  in  $n = 4$ , is reached with an odd number of photons (minimum of five photons here). This path is preferable to the maximal angular momentum,  $\ell = 1$ , that could be reached with an odd number of photons in an  $n = 3$  state. This behavior is reminiscent of the dominance of  $4f$  and higher  $f$ -state contributions in atomic ionization in hydrogen and xenon at 600 and 800 nm, where a similar preference appears [46]. We

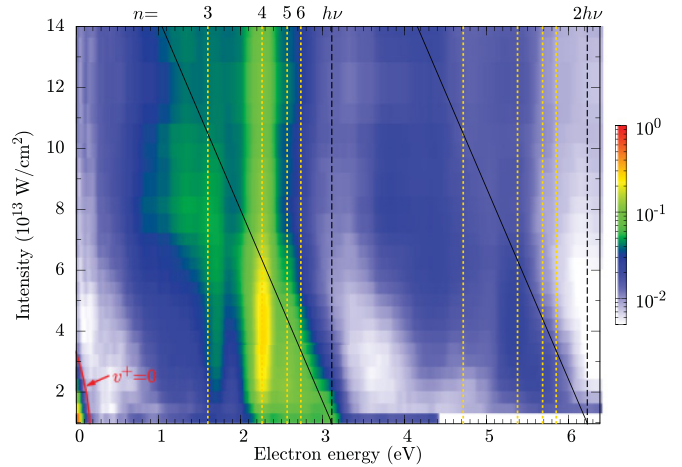


FIG. 9. (Color online) Map of the intensity-dependent photoelectron energy distribution at a wavelength of 398 nm. The momentum spectra were integrated over a  $\pm 20^\circ$  range around the polarization axis, each spectrum being area normalized. Note that this wavelength is different from those of Figs. 8 and 10, 396 nm, resulting in a significantly different appearance of lowest-energy electrons.

conclude that the dynamic system preferentially accesses the highest angular momentum state. As an odd number of photons is used to populate the intermediate at 398 nm, this must be an even principal quantum number state.<sup>2</sup>

Commensurate with this identification of molecular  $4f$  intermediate states is the angular distribution from the resonant intermediate in  $(5 + 1)$ -photon ionization at 396 nm; see Fig. 10(c). The angular distribution of photoelectrons in this channel confirms the distinct  $g$  character,  $\ell = 4$ .

<sup>2</sup>On this basis one might argue that even higher even  $n$  values should appear in the spectra. Their relative absence is due to the diminution of excitation probability, which should roughly follow the  $1/n^3$  rule.

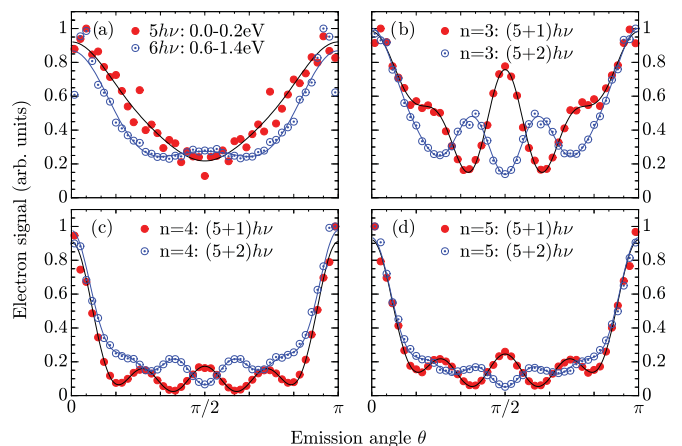


FIG. 10. (Color online) Angular distributions at 396 nm. (a) is taken at  $2 \times 10^{13}$  W/cm<sup>2</sup>. The lowest-energy contribution from five-photon NRI and from RI via the  $E,F$  ( $v = 0$ ) state is shown with solid red dots, and the NR six-photon channel is shown with blue circled dots. (b)–(d) were recorded at  $4 \times 10^{13}$  W/cm<sup>2</sup>. They give the signatures from resonant intermediate states in  $n = 3, 4, 5$  in the lowest and first ATI channel.

The electron energy map in Fig. 9 also reveals the ponderomotively dominated channel closing of six- and seven-photon nonresonant ionization, as indicated by the slanted black lines. In Fig. 10(a) the prominent  $p$  character,  $\ell = 1$ , appears at the lowest electron energies, commensurate with one-photon ionization of the  $E,F$  ( $v = 0$ ) level and with five-photon nonresonant ionization. The signature at the higher electron energy in Fig. 10(a) corresponds to nonresonant six-photon ionization, showing the appropriate change in angular pattern.

In Figs. 10(b)–10(d), the angular signatures from ionization of molecular Rydberg states with  $n = 3, 4, 5$  are shown. In each case, the number of nodes in the spectra is commensurate with the number of photons involved, considering the initial  $\ell = 0$  electron. A concentration of emission along the laser polarization axis with increasing  $n$  value is apparent. This is a consequence that ever-higher  $\ell$  states can be admixed at increasing  $n$  values.

### C. Wavelengths between 470 and 545 nm

A representative sample of spectra in this range of wavelengths is given in Fig. 11. We have discussed the case at 470 nm in detail in a previous paper [48]. Similar conclusions apply to the entire wavelength range shown in Fig. 11.

The dominant intermediate states are the  $H\bar{H}$ ,  $P$ , and  $O$  states, which undergo strong nonponderomotive ac Stark shifting. Angle-integrated spectra are given in Fig. 12.

In this representation of the data the nonponderomotive dynamics manifest in the form of rather broad resonance peaks, especially for  $n = 3$ . We also mark in Fig. 12 (red bars) contributions from nonresonant ionization with seven photons. These overlap with the signal from resonant ionization.

We recognize that as the photon number used in the ionization process changes by 1 so does the number of nodal planes, commensurate with the additional angular momentum imparted in the system. This finding is also evident from the angular distributions, examples of which are given in Fig. 13.

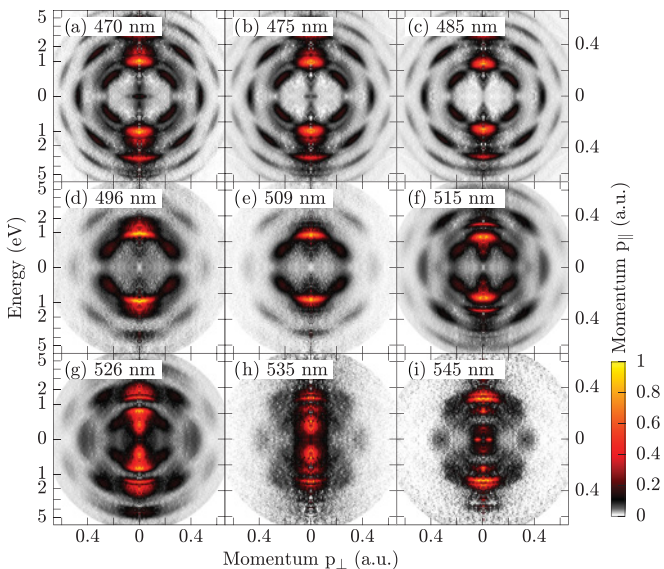


FIG. 11. (Color online) Photoelectron momentum maps recorded at various wavelengths from 470 to 545 nm at  $\mathcal{I} \approx 10^{13}$  W/cm<sup>2</sup>.

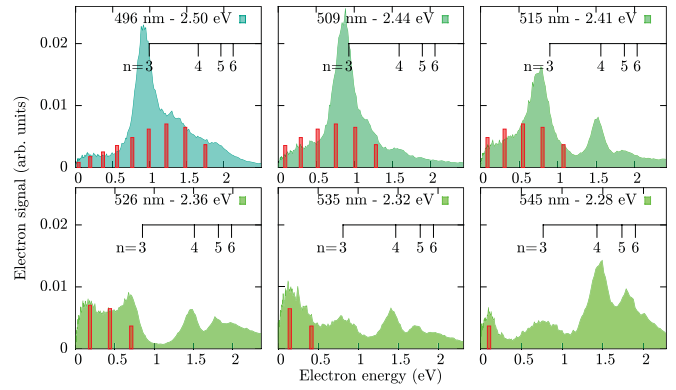


FIG. 12. (Color online) Angle-integrated spectra for  $\lambda = 496$ –545 nm at  $\mathcal{I} \approx 10^{13}$  W/cm<sup>2</sup>. The energies expected from nonresonant ionization are marked as red bars, with their height representing the ground-state  $\text{H}_2 \rightarrow \text{H}_2^+$  Frank-Condon factors.

At these longer wavelengths the higher-order ATI peaks become significantly more prominent. The ATI features and complex angular distributions are readily identified in the map of emission angle versus electron energy; see the case for 470 nm shown in Fig. 14. A most prominent feature is the curved islands of intensity in the region between 1 and 2 eV; see Fig. 14.

If we stick with the general notion that higher intensity means lower electron energy, the curvature suggests that higher angular momenta contribute to the features here as the intensity rises. A decomposition into the partial waves  $\ell = 0, 1, 2, 3$ , according to Eq. (4), is shown in Fig. 15.

The changes of the  $\beta$  parameters with energy within the broad peak are evident. We attribute this behavior to nonponderomotive effects, induced by one-photon coupling between excited states of  $\text{H}_2$ ; however, our model calculation [48] was not able to fully reproduce the observed intensity pattern. This peculiar angular pattern is also prominent at all other wavelength shown in Fig. 11; all plots show noncircular angular distributions.

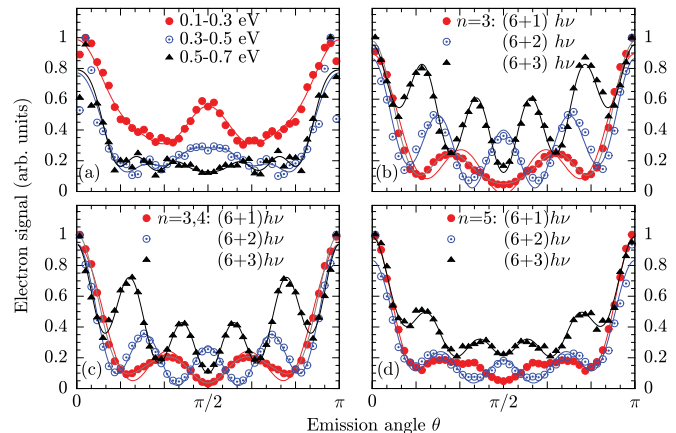


FIG. 13. (Color online) Angular distributions for selected energies at 470 nm are shown in (a). The change in angular momentum with increasing ATI order is clearly visible in (b)–(d).

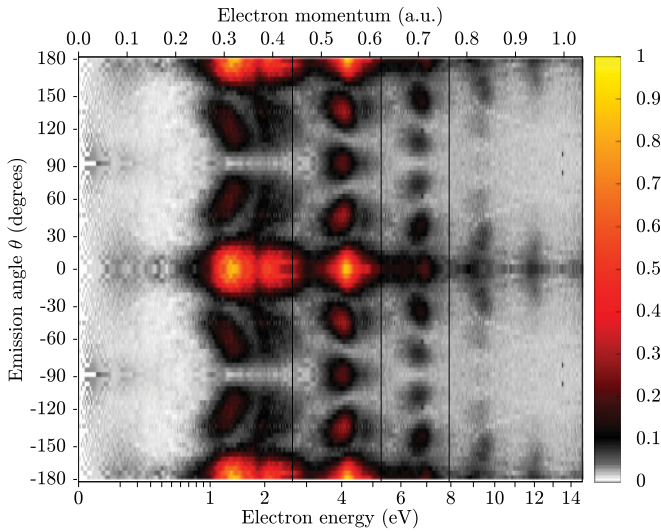


FIG. 14. (Color online) Angle-resolved electron momentum distribution at 470 nm. The black lines refer to one-, two-, and three-photon energies,  $h\nu = 2.64$  eV.

#### D. Wavelengths near 800 nm

Spectra were recorded at a center wavelength of 800 nm at intensities up to  $1.5 \times 10^{14}$  W/cm<sup>2</sup> using the setup of Fig. 3 but with a homogeneous electric field of 200 V/cm. Results at fixed peak intensities are shown in Fig. 16. Figure 17 gives the intensity dependence, integrated over a small range of angles,  $0^\circ$ – $20^\circ$ . The Keldysh parameter,

$$\gamma = \sqrt{I_P/2U_P}, \quad (5)$$

where  $I_P$  signifies the ionization potential of molecular hydrogen and  $U_P$  is the ponderomotive potential, varies from  $\gamma = 2.5$  to  $\gamma = 1.1$  in Fig. 17. The higher nonlinearity arising from the higher photon number results in more complex spectral features; however, the natural simplification of spectra, according to Eq. (3), also occurs at this wavelength. At 800 nm nominally a minimum of 10 photons are needed

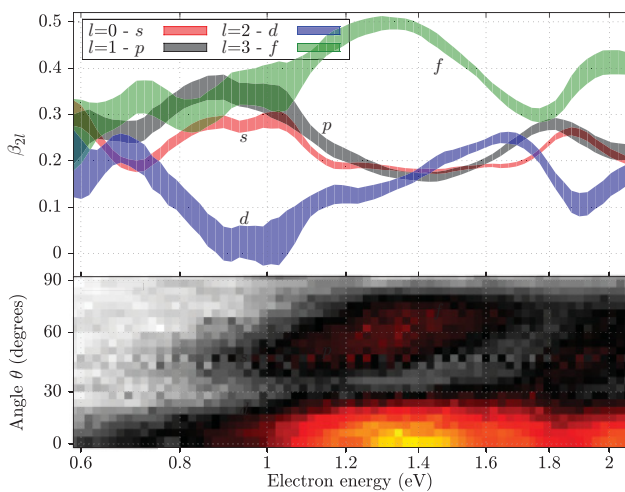


FIG. 15. (Color online) A section of the data in Fig. 14 is shown together with the development of beta parameters  $\beta_{2l}$  according to Eq. (4).

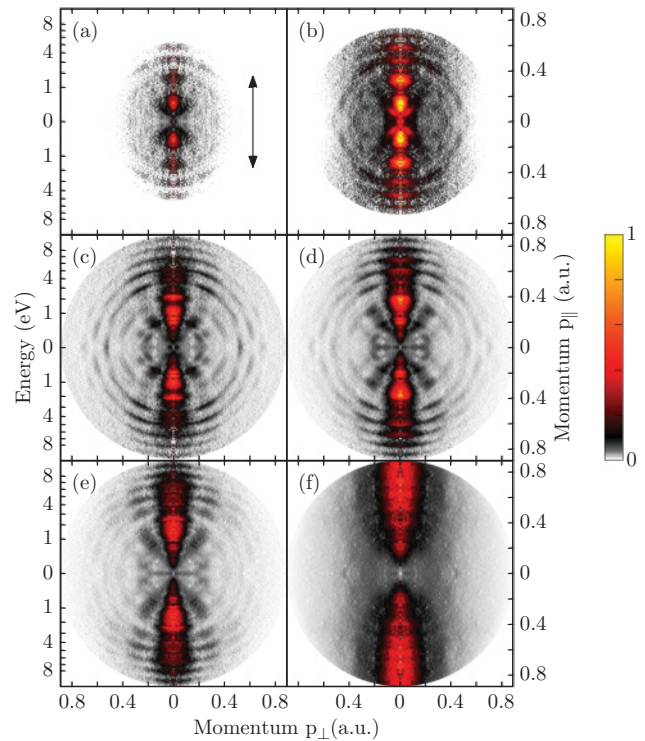


FIG. 16. (Color online) Photoelectron momentum maps at  $\lambda = 800$  nm recorded at intensities of (a) 2.4, (b) 2.6, (c) 3.7, (d) 4.7, (e) 5.8, and (f)  $15 \times 10^{13}$  W/cm<sup>2</sup>.

for ionization, but at least 11 photons are needed at practical experimental intensities due to ponderomotive shifting of the ionization potential.

The structured spectral contributions at electron energies below the one-photon energy indicate resonant multiphoton processes. A closer look reveals that the observed peaks merely shift with intensity, a clear signature for the resonant character of the underlying ionization processes. As a guide to the

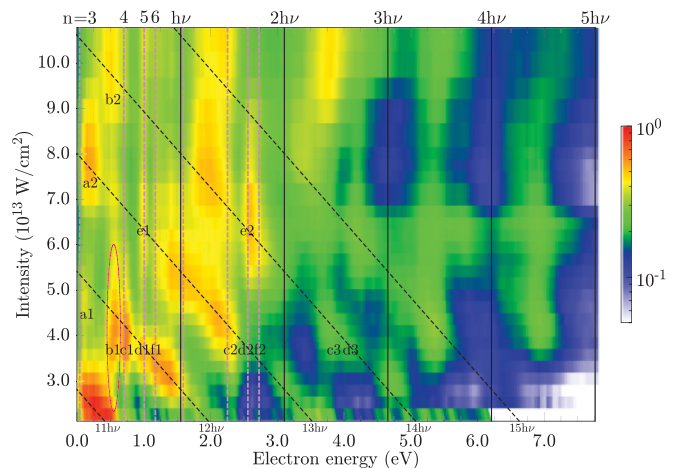


FIG. 17. (Color online) Photoelectron energy spectra retrieved from Fig. 16, summed up over  $\pm 20^\circ$  around the polarization axis and area normalized at each intensity. The lowercase identifications of the islands refer to Figs. 18(a)–18(f), and the number refers to the consecutive traces in these.

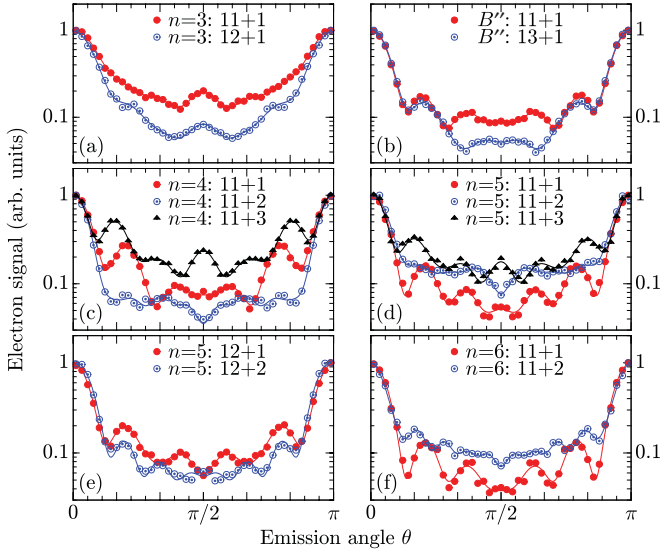


FIG. 18. (Color online) Angular distributions at  $\lambda = 800$  nm. Electron energies and laser intensities for each data set may be read from the labels a1–f2 marked in Fig. 17.

eye we include in Fig. 17 slanted dashed lines to locate the channel closings. The dashed red lines (vertical) mark islands of resonantly enhanced intermediate states. These states are identified with a lowercase letter signifying the intermediate resonance (see caption of Fig. 18) and a consecutive number. A further point of evidence for the prevalence of multiphoton ionization is the switching of the number of nodes in the angular distribution by 1 for subsequent ATI peaks; see Fig. 18.

Most of the observed resonance structures can be explained within the principle of spectral simplification, as both kinetic energies and angular distributions (Fig. 18) support the assignment of the principle quantum number  $n$ .

A contribution of resonant character, at  $\sim 0.54$  eV, does not, however, comply with this simple rule; see the red ellipse labeled b1 in Fig. 17. We attribute this additional resonance to  $(11 + 1)$ -photon RI via the  $B''$  ( $4p\sigma$ ) state rather than to  $(8 + 3)$ -photon RI via vibrational levels of the  $B$  state, as previously assumed [56]. A simulation of spectra assuming Franck-Condon-like transitions and ponderomotive shifting of excited states is included in Fig. 19. Ionization via the  $B''$  state is governed by larger FC factors than ionization via the  $B$  state and leads to a contribution in the correct energy range.

In a similar fashion the resonances at about 0.1 eV, labeled a1 and b1, can be attributed to ionization via the  $D$  and  $H$  states in  $(11 + 1)$ - and  $(12 + 1)$ -photon RI processes, respectively.

Contributions to the electron spectra from double ionization and dissociation of  $H_2$  and  $H_2^+$  followed by ionization of atomic hydrogen are, by comparison, negligible at 800 nm. We have carried out an independent coincidence measurement monitoring the appearance of electrons in coincidence with  $H_2^+$ . This coincidence experiment already shows all structures apparent in Figs. 16(a)–16(e); hence the double ionization channel at 800 nm is only a tiny contribution at intensities below  $10^{14}$  W/cm $^2$ .

The longer-duration laser cycle leads to a higher probability for tunneling, which is expected to begin to dominate at

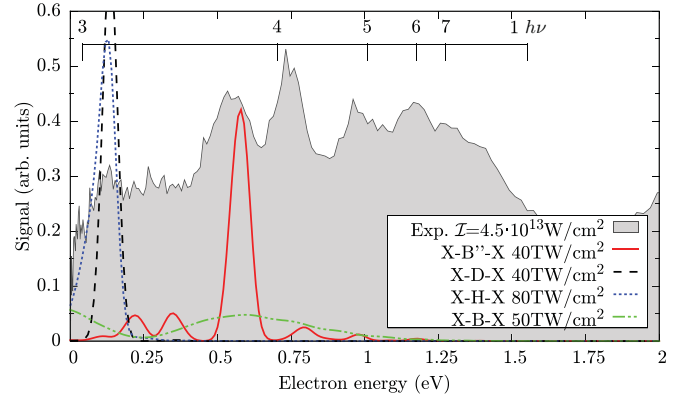


FIG. 19. (Color online) Modeled electron spectra for ionization via vibrational levels of the states  $B$ ,  $B''$ ,  $D$ , and  $H$ . Spectra show release energies on basis of FC-like transitions and ponderomotive shifting. Electronic rates are taken to be equal in this simulation. The angle-integrated experimental spectrum at  $4.5 \times 10^{13}$  W/cm $^2$  is shown as the gray area.

the highest intensities that appear in Fig. 17. At intensities beyond approximately 80 TW/cm $^2$  the transition to tunneling is evident from the loss of resonance structures. What is unusual is the dominance of the second ATI peak over the first one at these higher intensities. We are unaware of a previous report on this in the literature.

## V. MODELING SPECTRA AND IONIZATION RATES

In the discussions above many simplified models for explaining certain experimental findings have already been introduced. In the following we concentrate on a more intimate discussion of the 400-nm spectra, on a discussion of the relationship between dominant angular momentum and principal quantum number state, and on a comparison of predicted and measured ionization rates.

### A. Dressed-state model near 400 nm

The primary excitation path at wavelengths near 400 nm is  $(5 + 1)$ -photon ionization involving intermediates of the lowest bound Rydberg $^3$  states with  $n = 3$  and 4. Figure 20 shows these resonant intermediate states at  $\lambda = 398$  nm, as calculated using the dressed-state model described in [48].

We see that dominant contributions arise from vibrational levels of the  $B4$  state ( $4f\sigma$ ). Resonances from  $B''$  ( $4p\sigma$ ) and  $D(3p\pi)$  are also present. On the other hand, the  $B'$  state ( $3p\sigma$ ) is dissociative at the five-photon energy and is not expected to contribute significantly to our photoelectron spectrum.

We may estimate the relative strength of the various resonance channels by comparing the relevant dipole transition matrix elements that appear in Fig. 21. To compare the relative strengths for excitation of  $B4$  and  $B''$  we consider the ratio

$$A_{B4B''} = \frac{a_{4f}}{a_{4p}} \propto \frac{\langle 4f|r|5d \rangle^2 + \langle 4f|r|5g \rangle^2}{\langle 4f|r|5d \rangle \langle 5d|r|4p \rangle}. \quad (6)$$

$^3$ Only at the lowest intensities is a weak four-photon channel open.

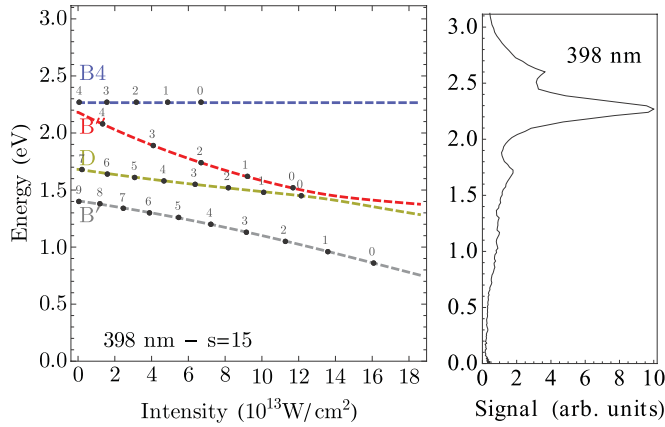


FIG. 20. (Color online) (left) Resonances predicted at 398 nm and (right) the experimental spectrum.

This ratio compares the summed amplitude products, which reach the final states  $4f$  and  $4p$  in stimulated absorption and emission via the  $5g$  and  $5d$  levels, following three-photon excitation of the virtual  $B4$  state; see Fig. 21.

In a hydrogenic approximation the right-hand term in Eq. (6) is 17.4. This consideration predicts that the electronic contribution from  $B''$  resonances is about  $17.4^2 \approx 300$  times smaller than the  $B4$  levels when both are prepared along the red arrows in Fig. 21.

It is more difficult to assess the relative strength of contributions from  $D(3p\pi)$ -state levels. We may invoke the proximity of the  $E, F \ ^1\Sigma_g^+(v=0)$  level to the four-photon transition and consider the relative strength of the transitions  $E, F \rightarrow D$  and  $E, F \rightarrow B''$ , as represented by the green arrows in Fig. 21. From Dressler and Wolniewicz [45] we find for the electronic dipole transition moments at an internuclear separation  $R = 2$  bohr,

$$d_{E,F \rightarrow D} = -1.91, \quad d_{E,F \rightarrow B''} = -0.84, \quad (7)$$

with the dipole transition  $E, F \rightarrow B4$  not being allowed in the hydrogenic approximation. When weighted with the detuning

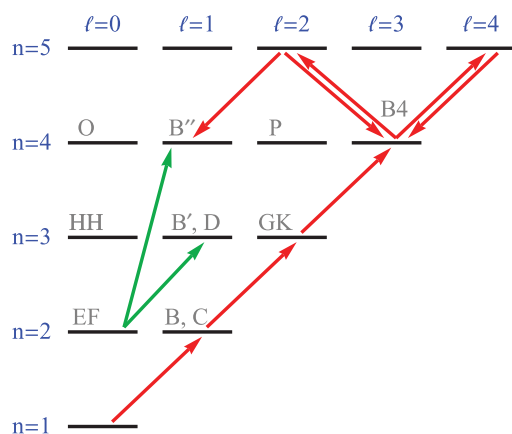


FIG. 21. (Color online) Dominant five-photon excitation paths at wavelengths near 400 nm.

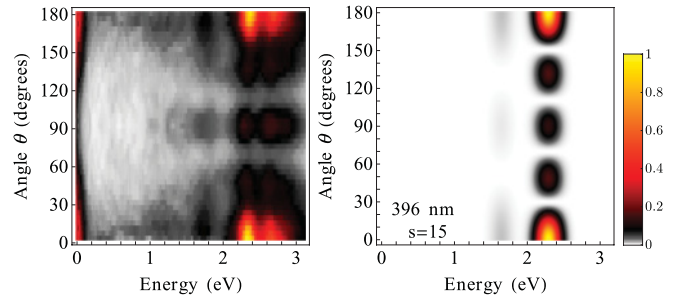


FIG. 22. (Color online) (left) Experimental data and (right) simulated photoelectron distribution for  $\lambda = 396$  nm at  $4 \times 10^{13}$  W/cm<sup>2</sup>. Note that the channels below 0.2 eV and above 2.5 eV are not part of the simulation model.

at 398 nm, we obtain for the ratio of excitation probabilities of  $B''$  and  $D$  states via  $E, F(v=0)$ ,

$$A_{B''D} = \frac{\sqrt{W_D - W_{E,F} - h\nu} d_{E,F \rightarrow B''}}{\sqrt{W_{B''} - W_{E,F} - h\nu} d_{E,F \rightarrow D}} \approx \frac{2}{5}. \quad (8)$$

Here  $W$  represents the respective state energies and  $h\nu$  is the photon energy.

No simple way appears by which we can relate the strength for four-photon transitions to the  $E, F$  state to four-photon transitions to  $5g$  or to three-photon transitions to  $B4$ . At  $4 \times 10^{13}$  W/cm<sup>2</sup> the experiment indicates a relative strength of signals from  $B4$ - and  $D$ -state resonances of  $\approx 4^2$ . We use this empirical calibration in the following. Combined with the result of Eq. (8) and neglecting the tiny contribution of  $B''$  excitation from (6), we predict for the electronic excitation amplitudes

$$B'' : D : B4 \approx 2 : 5 : 20. \quad (9)$$

The dominance of the contribution of the  $B4$  state is consistent with the *ab initio* prediction in [1], where this state is labeled as  $4 \ ^1\Sigma_u^+$ .

Application of this model to ionization at  $\lambda = 396$  nm at an intensity of  $\mathcal{I} = 4 \times 10^{13}$  W/cm<sup>2</sup> results in an electron distribution as shown in Fig. 22 (right). Evidently the energy and angular distribution of the peaks at  $\sim 1.7$  and  $\sim 2.3$  eV of the experimental data in Fig. 22(a) are predicted correctly with this model. Also the angular distribution predicted for the peak at 2.3 eV from  $(5 + 1)$ -photon ionization is in remarkable agreement with the experimental data; see the comparison in Fig. 23(a). For the resonances contributing to the peak near 1.65 eV our model obviously misses an important higher angular momentum contribution; see Fig. 23(b). We ran this simulation as a function of intensity and show at the top of Fig. 24 the predicted intensity dependence of the angle-integrated photoelectron spectrum for 398 nm. This result is in very good agreement with the experimental finding shown at the bottom of Fig. 24. Note that the triangular structure, beginning at 3.1 eV and extending to lower energies, is due to nonresonant six-photon ionization, a process that is not part of our model; the low-energy contribution,  $< 200$  meV, from nonresonant ionization with five photons is not part of our model either.

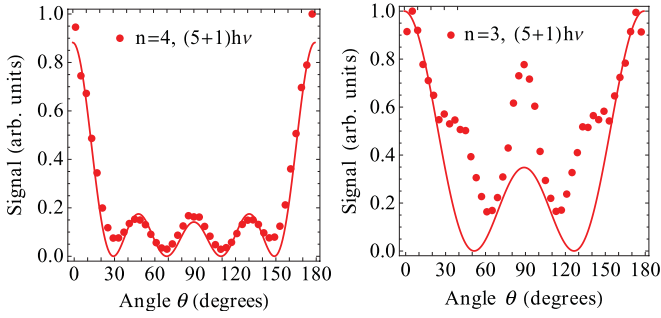


FIG. 23. (Color online) Predicted and observed angular distributions at 396 nm, at  $4 \times 10^{13}$  W/cm<sup>2</sup>. (a) The vibrational resonances of the  $B4^1\Sigma_u^+$  state (labeled  $n = 4$ ) at 2.3 eV and (b) the result labeled  $n = 3$  for the peak near 1.65 eV (resonances of the  $D^1\Pi_u$  and  $B''^1\Sigma_u^+$  states).

### B. Comparison of ionization rates with theory

Along with the data of Fig. 9 ionization rates were measured at intensities ranging from  $1 \times 10^{13}$  to  $1.5 \times 10^{14}$  W/cm<sup>2</sup> at a wavelength of 398 nm. In order to assure stable conditions during measurements, the pulse length of the fundamental beam was continuously monitored with a FROG device while a photodiode was used to monitor the power. Ions were detected with a channeltron in a time-of-flight setup, and the signal was digitized and recorded with a multievent time-to-digital converter (TDC) card (FAST Comtec P7886). Protons

and molecular ions were recorded separately. The proton contribution to the total ionization yield rises rapidly from 8% at  $10$  TW/cm<sup>2</sup> to 45% at  $40$  TW/cm<sup>2</sup>. Beyond this intensity the proton fraction appears to saturate, reaching  $55\% \pm 3\%$  at  $1.5 \times 10^{14}$  W/cm<sup>2</sup>.

To compare theoretical and experimental ionization yields the procedures outlined below were followed. The computation was done on a 40-cycle cos<sup>2</sup> field envelope; on the other hand, our experiment employed a 100-fs full width at half maximum (FWHM) pulse of intensity. The difference in pulse durations was incorporated by fitting the calculated yield  $Y(\mathcal{I}_0)$  with a power law,

$$Y(\mathcal{I}_0) = \sigma_k \tau_{\text{eff}} \left( \frac{\mathcal{I}_0}{\hbar\omega} \right)^k, \quad (10)$$

where  $\sigma_k$  denotes a generalized cross section of order  $k$  and  $\mathcal{I}_0$  is the peak intensity. A fit of the theoretical result to Eq. (10) gives  $\sigma_k = 1.17 \times 10^{-122} \text{cm}^{2k} \text{s}^{k-1}$  and  $k = 4.16$ . With  $\tau_{\text{eff}}$  we characterize an effective interaction time for a given pulse envelope  $f(t)$  and order of nonlinearity  $k$  according to

$$Y(\mathcal{I}_0) = \int dt \sigma_k \frac{\mathcal{I}(t)^k}{(\hbar\omega)^k} = \sigma_k \left( \frac{\mathcal{I}_0}{\hbar\omega} \right)^k \underbrace{\int f^k(t) dt}_{\tau_{\text{eff}}}. \quad (11)$$

The values found above for  $\sigma_k$  and  $k$  were then used to predict values of  $Y$  in (11) for our experimental pulse shape with

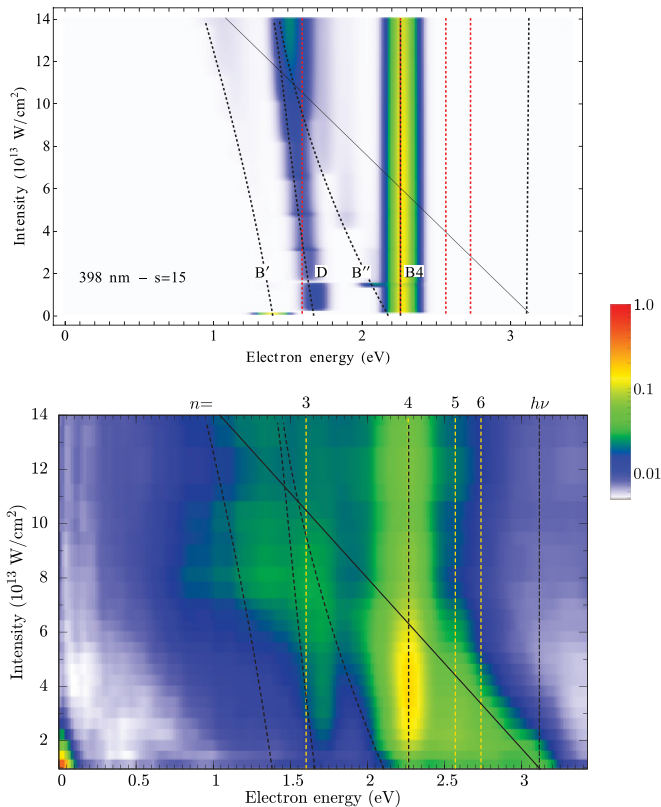


FIG. 24. (Color online) Map of the intensity-dependent photoelectron energy distribution at a wavelength of 398 nm from (top) the model calculation and (bottom) the experiment. The black dashed lines indicate the shifting of relevant potentials according to Fig. 20.

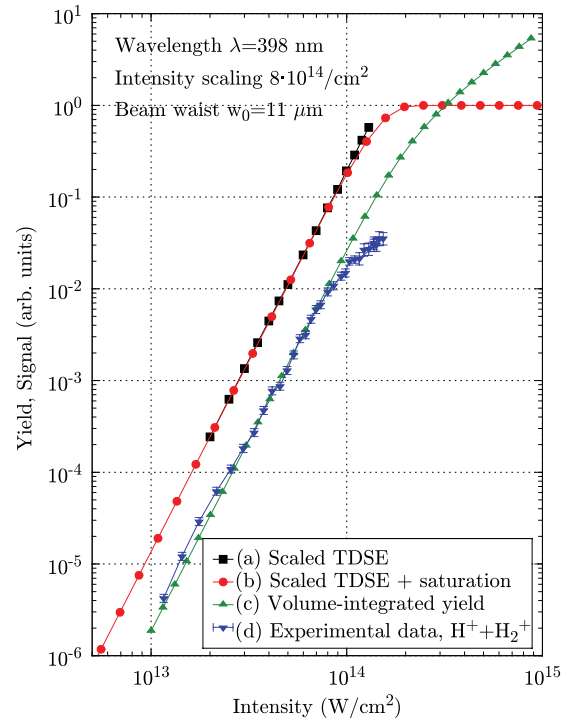


FIG. 25. (Color online) The ionization yield of  $\text{H}_2$  at 398 nm is shown on an absolute scale common to all results. Trace a gives the result of Ref. [1] scaled to a laser pulse duration of 100-fs FWHM. Trace b shows the result of trace a, including saturation. Trace c results from integration of trace b over a Gaussian focus with  $w_0 = 11 \mu\text{m}$ . The data set d represents experimental data on a peak intensity scale. The deviation of experiment from theory at the highest intensities is attributed to saturation of the ion-counting detector.

a length of 100 fs. This results in a yield of  $Y = 0.011$  at an intensity of  $\mathcal{I}_0 = 5 \times 10^{13}$  W/cm<sup>2</sup> and  $Y = 0.2$  at  $\mathcal{I}_0 = 10^{14}$  W/cm<sup>2</sup>, respectively.

In this fashion the data shown as trace a in Fig. 25 were constructed. The experimental intensity distribution over the ionization volume and saturation of the ionization process are not yet accounted for. Upon including saturation of the ionization of the neutral molecule sample trace b is obtained. Finally, in order to accommodate the experimental intensity distribution in the laser focus, we integrate the yield according to

$$S(\mathcal{I}_{\text{peak}}) = \int_0^{\mathcal{I}_{\text{peak}}} d\mathcal{I}_0 Y(\mathcal{I}_0) \frac{dV}{d\mathcal{I}_0}, \quad (12)$$

where  $\mathcal{I}_0$  is the local peak intensity and  $\mathcal{I}_{\text{peak}}$  is the peak intensity in the center of the focus. The volumetric weighting factor  $dV/d\mathcal{I}$  is given as [57]

$$\frac{dV}{d\mathcal{I}} = V_{\text{eff}} \frac{2\mathcal{I} + \mathcal{I}_{\text{peak}}}{3\mathcal{I}^2} \sqrt{\frac{\mathcal{I}_{\text{peak}}}{\mathcal{I}} - 1}, \quad (13)$$

where

$$V_{\text{eff}} = \pi w_0^2 z_R \quad (14)$$

denotes the effective volume of the laser focus characterized by the waist  $w_0$  and the Raleigh length  $z_R$ . The effective volume is at this stage merely a multiplicative factor to which we return below. The theoretically predicted result including saturation and focus-volume integration is shown as trace c in Fig. 25.

This result closely matches trace d, the experimental result, which is the summed signal of protons and H<sub>2</sub><sup>+</sup> ions from the time-of-flight (TOF) measurements, normalized to the gas pressure.

No substructures appear in the experimental data for the ionization rate within the experimental error. In the calculation [1] pronounced substructures from the individual resonance channels appear in the ionization rate along the internuclear distance and intensity scales; these disappear already upon summing over internuclear distance in the theoretical ionization rate.

The experimental data shown as trace d were obtained by scaling the observed event rate by a factor of  $1/(2.414 \times 10^{22} \text{ mbar})$  for conversion from (events/mbar/pulse) to (events/pulse) using the ideal gas law with  $T = 300$  K. In order to calibrate the laser intensity scale, the measured values of laser power were scaled by  $8 \times 10^{14}$  W/cm<sup>2</sup>. This factor was deduced from the observation of channel closing in Fig. 9 and is consistent with the resonance channels discussed throughout this paper. For the absolute comparison of the yields from theory and experiment, the explicit focal volume needs to be specified. Rather than following this path to an absolute comparison, we deduce the scale of the effective volume in a

comparison to theory, using the ideal Gaussian beam value of the Raleigh length,  $z_R = \pi w_0^2/\lambda$ . Then the waist  $w_0$  remains as the sole parameter left between the absolute event rate per pulse between theory and experiment. Note that  $w_0$  enters at the fourth power in this comparison.

Assuming unity detection efficiency for ions in our experiment, we find *quantitative* agreement between the prediction of Vanne and Saenz [1] and our experiment for  $w_0 = 11 \mu\text{m}$ . We were unable to determine *in situ* an experimental value for  $w_0$  in the focusing setup used in this experiment. However, the same laser, in similar setups in our laboratory, provided values of  $w_0 = 18 \pm 2 \mu\text{m}$  at twice the wavelength used here. This suggests that  $w_0 = 11 \mu\text{m}$  is indeed a reasonable value. We are therefore led to claim that our experiment delivers quantitative confirmation of the *absolute* rates predicted in [1]. We consider this agreement to be a tribute to the reliability and meaningfulness of their nonperturbative treatment of the full time-dependent Schrödinger equation for both correlated electrons. Keeping in mind that the experimental data were taken at a considerably longer pulse duration, the agreement in the slope of the ionization rate is already remarkable. Even more gratifying is the purposeful comparison of absolute yields.

## VI. CONCLUSION

We show that single ionization of molecular hydrogen in a strong linearly polarized laser field can be interpreted in quantitative models that account for the excited-state structure of the molecule, its energetic deformation by the ac Stark effect, and that make use of hydrogen-like selection rules in the transition probabilities among the Rydberg states. This framework is shown to be valid over the range from 300 to 800 nm, with the results being corroborated in the observed photoelectron energy and angular patterns. These findings also show that only at the longer wavelengths and only at intensities exceeding  $10^{14}$  W/cm<sup>2</sup> is the multiphoton process superseded by tunneling phenomena.

We succeeded in a near-absolute comparison of measured ionization yields at 398 nm with the predictions based on a numerical solution of the time-dependent Schrödinger equation for two correlated electrons [1]. The large database from the experiments described here is available in digital form for testing advanced theories on molecular strong-field ionization.

## ACKNOWLEDGMENTS

This work was supported by the Deutsche Forschungsgemeinschaft under Grant No. HE-2525/6 and by the Marie Curie ITN ICONIC.

- [1] Y. V. Vanne and A. Saenz, *Phys. Rev. A* **79**, 023421 (2009).  
 [2] S. Chelkowski, T. Zuo, O. Atabek, and A. D. Bandrauk, *Phys. Rev. A* **52**, 2977 (1995).  
 [3] A. Apalategui and A. Saenz, *J. Phys. B* **35**, 1909 (2002).  
 [4] M. Awasthi, Y. V. Vanne, A. Saenz, A. Castro, and P. Decleva, *Phys. Rev. A* **77**, 063403 (2008).

- [5] Y. V. Vanne and A. Saenz, *J. Mod. Opt.* **55**, 2665 (2008); *Phys. Rev. A* **82**, 011403 (2010).  
 [6] K. Harumiya, I. Kawata, H. Kono, and Y. Fujimura, *J. Chem. Phys.* **113**, 8953 (2000).  
 [7] K. Harumiya, H. Kono, Y. Fujimura, I. Kawata, and A. D. Bandrauk, *Phys. Rev. A* **66**, 043403 (2002).

- [8] L. A. A. Nikolopoulos, T. K. Kjeldsen, and L. B. Madsen, *Phys. Rev. A* **76**, 033402 (2007).
- [9] C. Cornaggia, D. Normand, J. Morellec, G. Mainfray, and C. Manus, *Phys. Rev. A* **34**, 207 (1986).
- [10] S. W. Allendorf and A. Szöke, *Phys. Rev. A* **44**, 518 (1991).
- [11] B. L. G. Bakker, D. H. Parker, and W. J. van der Zande, *Phys. Rev. Lett.* **86**, 3272 (2001).
- [12] A. S. Alnaser, T. Osipov, E. P. Benis, A. Wech, B. Shan, C. L. Cocke, X. M. Tong, and C. D. Lin, *Phys. Rev. Lett.* **91**, 163002 (2003).
- [13] J. H. Posthumus, *Rep. Prog. Phys.* **67**, 623 (2004).
- [14] X. Urbain, B. Fabre, V. M. Andrianarijaona, J. Jureta, J. H. Posthumus, A. Saenz, E. Baldit, and C. Cornaggia, *Phys. Rev. Lett.* **92**, 163004 (2004).
- [15] W. Vanroose, F. Martin, T. N. Rescigno, and C. W. McCurdy, *Science* **310**, 1787 (2005).
- [16] Th. Ergler, B. Feuerstein, A. Rudenko, K. Zrost, C. D. Schröter, R. Moshhammer, and J. Ullrich, *Phys. Rev. Lett.* **97**, 103004 (2006).
- [17] C. Beylerian, S. Saugout, and C. Cornaggia, *J. Phys. B* **39**, L105 (2006).
- [18] M. R. Thompson, M. K. Thomas, P. F. Taday, J. H. Posthumus, A. J. Langley, L. J. Frasinski, and K. Codling, *J. Phys. B* **30**, 5755 (1997).
- [19] G. N. Gibson, M. Li, C. Guo, and J. Neira, *Phys. Rev. Lett.* **79**, 2022 (1997).
- [20] D. Pavicic, A. Kiess, T. W. Hansch, and H. Figger, *Phys. Rev. Lett.* **94**, 163002 (2005).
- [21] A. Rudenko, B. Feuerstein, K. Zrost, V. L. B. de Jesus, T. Ergler, C. Dimopoulou, C. D. Schroter, R. Moshhammer, and J. Ullrich, *J. Phys. B* **38**, 487 (2005).
- [22] S. Saugout, E. Charron, and C. Cornaggia, *Phys. Rev. A* **77**, 023404 (2008).
- [23] B. Manschwetus, T. Nubbemeyer, K. Gorling, G. Steinmeyer, U. Eichmann, H. Rottke, and W. Sandner, *Phys. Rev. Lett.* **102**, 113002 (2009).
- [24] A. Staudte *et al.*, *Phys. Rev. Lett.* **102**, 033004 (2009).
- [25] H. Pummer, H. Egger, T. S. Luk, T. Srinivasan, and C. K. Rhodes, *Phys. Rev. A* **28**, 795 (1983).
- [26] N. Bjerre, R. Kachru, and H. Helm, *Phys. Rev. A* **31**, 1206 (1985).
- [27] D. W. Chandler and L. R. Thorne, *J. Chem. Phys.* **85**, 1733 (1986).
- [28] R. R. Freeman, P. H. Bucksbaum, and T. J. McIlrath, *IEEE J. Quantum Electron.* **24**, 1461 (1988).
- [29] H. Rottke, J. Ludwig, and W. Sandner, *Phys. Rev. A* **54**, 2224 (1996).
- [30] J. H. Posthumus, B. Fabre, C. Cornaggia, N. de Ruette, and X. Urbain, *Phys. Rev. Lett.* **101**, 233004 (2008).
- [31] H. Helm, M. J. Dyer, and H. Bissantz, *Phys. Rev. Lett.* **67**, 1234 (1991).
- [32] J. W. J. Verschuur, L. D. Noordam, and H. B. van Linden van den Heuvell, *Phys. Rev. A* **40**, 4383 (1989).
- [33] M. A. O'Halloran, S. T. Pratt, P. M. Dehmer, and J. L. Dehmer, *J. Chem. Phys.* **87**, 3288 (1987).
- [34] W. L. Glab and J. P. Hessler, *Phys. Rev. A* **35**, 2102 (1987).
- [35] W. L. Glab and J. P. Hessler, *Phys. Rev. A* **42**, 5486 (1990).
- [36] S. W. Allendorf and A. Szöke, *Phys. Rev. A* **44**, 518 (1991).
- [37] L. J. Lembo, D. L. Huestis, S. R. Keiding, N. Bjerre, and H. Helm, *Phys. Rev. A* **38**, 3447 (1988).
- [38] E. Y. Xu, H. Helm, and R. Kachru, *Phys. Rev. A* **39**, 3979 (1989).
- [39] B. W. Boreham and B. Luther-Davis, *J. Appl. Phys.* **50**, 2533 (1979).
- [40] R. R. Freeman, P. H. Bucksbaum, H. Milchberg, S. Darack, D. Schumacher, and M. E. Geusic, *Phys. Rev. Lett.* **59**, 1092 (1987).
- [41] P. Agostini, J. Kupersztych, L. A. Lompre, G. Petite, and F. Yergeau, *Phys. Rev. A* **36**, 4111 (1987).
- [42] M. Saeed, M. J. Dyer, and H. Helm, *Phys. Rev. A* **49**, 1491 (1994).
- [43] B. Witzel, H. Schröder, S. Kaesdorf, and K.-L. Kompa, *Int. J. Mass Spectrom. Ion Phys.* **172**, 229 (1998).
- [44] K. Dressler and L. Wolniewicz, *J. Mol. Spectrosc.* **96**, 195 (1982).
- [45] K. Dressler and L. Wolniewicz, *Ber. Bunsen-Ges.* **99**, 246 (1995).
- [46] H. Rottke, B. Wolff-Rottke, D. Feldmann, K. H. Welge, M. Dörr, R. M. Potvliege, and R. Shakeshaft, *Phys. Rev. A* **49**, 4837 (1994).
- [47] V. Schyja, T. Lang, and H. Helm, *Phys. Rev. A* **57**, 3692 (1998).
- [48] T. Wilbois and H. Helm, *Phys. Rev. A* **83**, 053414 (2011).
- [49] H. Helm, N. Bjerre, M. J. Dyer, D. L. Huestis, and M. Saeed, *Phys. Rev. Lett.* **70**, 3221 (1993).
- [50] A. T. J. B. Eppink and D. H. Parker, *Rev. Sci. Instrum.* **68**, 3477 (1997).
- [51] C. Bordas, F. Pauling, H. Helm, and D. L. Huestis, *Rev. Sci. Instrum.* **67**, 2257 (1996).
- [52] Ch. Jungen and O. Atabek, *J. Chem. Phys.* **66**, 5584 (1977).
- [53] K. Reid, *Annu. Rev. Phys. Chem.* **54**, 397 (2003).
- [54] U. Fantz and D. Wuenderlich, *At. Data Nucl. Data Tables* **92**, 853 (2006).
- [55] K. P. Huber and G. Herzberg, *Molecular Spectra and Molecular Structure* (Van Nostrand Reinhold, New York, 1979), Vol. IV.
- [56] T. Wilbois and H. Helm, *Laser Physics* **18**, 579 (2008).
- [57] P. Wang *et al.*, *Opt. Lett.* **30**, 664 (2005).